Atmospheric Environment 309 (2023) 119939

Contents lists available at ScienceDirect

Atmospheric Environment

journal homepage: www.elsevier.com/locate/atmosenv

Synoptic meteorological conditions and contributing factors to air quality during the SIJAQ campaign

Cheol-Hee Kim[a,b,*], Hyun-Young Jo[b], Yu-Jin Jo[c], Hyo-Jung Lee[a], Jong-Min Kim[a], Na-Mi Lee[d], So-Yeon Jeong[e], Seung-Hee Baek[a], Min-Jun Park[a], Lim-Seok Chang[f,**], Jong-Jae Lee[g], Chang-Keun Song[g,h,***]

[a] Department of Atmospheric Sciences, Pusan National University, Busan, 46241, Republic of Korea
[b] Institute of Environmental Studies, Pusan National University, Busan, 46241, Republic of Korea
[c] Department of Environmental Engineering Science, University of Florida, Gainesville, FL, 32611, USA
[d] Center of Remote Sensing and GIS, Korea Polar Research Institute (KOPRI), Incheon, 21990, South Korea
[e] Numerical Modeling Center, Korea Meteorological Administration, Daejeon, 35208, Republic of Korea
[f] Environmental Satellite Center, National Institute of Environmental Research, Incheon, 22689, Republic of Korea
[g] Department of Urban and Environmental Engineering, Ulsan National Institute of Science and Technology (UNIST), Ulsan, 44919, Republic of Korea
[h] Graduate School of Carbon Neutrality, Ulsan National Institute of Science and Technology (UNIST), Ulsan, 44919, Republic of Korea

HIGHLIGHTS

- SIJAQ campaign was conducted in 2021 for GEMS validation.
- Synoptic features are presented over SMA for the entire SIJAQ campaign.
- Local emission vs. external transport were contrasted during the campaign.

ARTICLE INFO

Keywords:
SIJAQ campaign
Transboundary transport process
Seoul metropolitan area
Synoptic meteorological conditions

ABSTRACT

The Satellite Integrated Joint Monitoring of Air Quality (SIJAQ) field campaign was conducted from October 10 to November 25, 2021, to assess air quality across the Korean Peninsula and validate the results of the Geostationary Environment Monitoring Spectrometer (GEMS) employing remote sensing, modeling, and satellite, aircraft, and ground measurements. To integrate all measurements collected during the campaign, synoptic features across the Korean Peninsula were analyzed. We identified cyclones and anticyclones by tracing weather charts and divided the campaign into five periods (P1 to P5): P1 - Sustained marine stagnation (October 10–28, 2021), P2 - Transitional stagnant high (October 29–November 7, 2021), P3 - Continental migratory low (November 8–14, 2021), P4 - Continental migratory high (November 15–21, 2021), and P5 - Continental migratory low (November 22–25, 2021). The synoptic features, such as the locations of stagnant or migratory cyclones and anticyclones were analyzed during the periods, in association with levels of particulate matter with a diameter of less than 2.5 μm ($PM_{2.5}$ levels) over the Seoul metropolitan area (SMA). The synoptic characteristics showed that the presence of a high pressure system was well associated with the occurrence of high $PM_{2.5}$ level over the SMA, and a pattern of near-surface divergence and descending motions originating from the mid-troposphere. In addition, we identified and compared two $PM_{2.5}$ level peaks caused by local accumulation and transboundary transport process. We also investigated the underlying synoptic meteorological mechanisms of these peaks in terms of large-scale dynamic variables, such as geostrophic wind speed, transient synoptic scale features, vorticity, and vorticity advection at 850 hPa geopotential height, which are responsible for transboundary transport and local accumulation-driven process of $PM_{2.5}$ in the SMA.

* Corresponding author. Department of Atmospheric Sciences, Pusan National University, San 30, Jangjeon-Dong, Geumjeong-Gu, Busan, 609-735, South Korea
** Corresponding author.
*** Corresponding author.
E-mail addresses: chkim2@pusan.ac.kr (C.-H. Kim), lschang@korea.kr (L.-S. Chang), cksong@unist.ac.kr (C.-K. Song).

https://doi.org/10.1016/j.atmosenv.2023.119939
Received 3 April 2023; Received in revised form 30 June 2023; Accepted 1 July 2023
Available online 7 July 2023

1. Introduction

The Geostationary Environment Monitoring Spectrometer (GEMS), which observes air quality from a Geostationary Earth Orbit (GEO), was successfully launched in early 2020 following the comprehensive ground and aircraft air quality measurement campaign (KORUS-AQ) conducted from 1 May–12 June in 2016 across the Korean Peninsula (Crawford et al., 2021). GEMS provides hourly air quality information on both aerosols and gases at an unprecedented spatial resolution of 7 km × 8 km, allowing for the observation of key atmospheric constituents, including O_3, NO_2, SO_2, HCHO, and aerosols (Kim et al., 2020). The need to scientifically validate measurements taken by the GEMS across the Korean Peninsula prompted the GEMS Map of Air Pollution (GMAP) campaign (26 October – 18 December) in 2020 (Chang et al., 2022), and the Satellite Integrated Joint Monitoring of Air Quality (SIJAQ) campaign (10 October–25 November) in 2021. The campaigns employed multi-perspective observations, including ground, remote sensing, and aircraft observations, as well as improvement techniques for emissions and emissions modeling across the Korean Peninsula to explore solutions to unresolved air pollution problems in the Seoul Metropolitan Area (SMA).

The present study focuses on the SMA, which is particularly susceptible to transboundary transport of air pollutants from downwind multi-source areas of Asian air pollutants under prevailing westerlies, such as eastern China, which has higher O_3 and Particulate Matter (PM) levels than the western region and frequently exceeds ambient air quality standards (Zhang et al., 2016; Zhao et al., 2017). Thus, transboundary transport of upstream continental outflow is an important factor for the air quality of downstream areas such as the SMA in northeastern Asia (Lee et al., 2022; Park et al., 2005). In association with transboundary transport process, many previous studies pointed out that meteorological factors play an important role across northeastern Asia (Peterson et al., 2019; Jo and Kim, 2013; Levin et al., 2005; Sun et al., 2006; Wang et al., 2006; Oh et al., 2010; Kim et al., 2011, 2021; Lee et al., 2019a,b). Following the diversification of remote-sensing measurements, modeling researches on investigating this impact are increasing (Park et al., 2020; Lee et al., 2014). Recent modeling and monitoring studies have shown that lower-tropospheric flow at around 1.5–3.0 km can be used to characterize transboundary transport process of air pollutants over northeastern Asia, reflecting the influence of large semi-permanent anticyclones (Kim et al., 2018; Lee et al., 2019a,b). Thus, meteorological factors primarily determine the extent to which transboundary transport of air pollutants can contribute to degraded air quality over the SMA and are important in interpreting air quality.

In this paper, we provide an overview of the meteorological conditions during the SIJAQ, carried out from October 10 to November 25, 2021. We investigated synoptic patterns and meteorological characteristics of the SMA during the entire SIJAQ campaign, as well as the meteorological factors associated with high $PM_{2.5}$ levels over the Korean Peninsula. We analyzed a vertical synoptic meteorological motions to identify air mass origin over the Korean Peninsula during the campaign, and assessed the meteorological synoptic factors influencing air pollution concentrations over the SMA. In particular, we divided the campaign period into several sub-periods and featured the synoptic conditions associated with cyclones and anticyclones. The features of stagnant or migratory cyclones and anticyclones were interpreted during the campaign in association with the air quality of the SMA.

2. Comprehensive measurements during the SIJAQ campaign

During the SIJAQ campaign, we obtained multi-perspective observations from the ground, air, and space, using remote sensing instruments such as the Multi-axis Differential Optical Absorption Spectrometer (Max-DOAS), the Compact Atmospheric Research - Differential Optical Absorption Spectrometer (CAR-DOAS), the Ground-based Common Data Acquisition System (GCAS), and the Pandora spectrometer. Here, we provide an overview of the meteorological characteristics during the campaign using synoptic weather charts and surface meteorological observations from the Automated Synoptic Observing System (ASOS) of the Korea Meteorological Administration (KMA). We discuss their associations with PM_{10} and $PM_{2.5}$ levels at surface Air Quality Monitoring (AQM) sites managed by the Korean Ministry of Environment across the SMA. The locations of the ASOS and AQM sites are shown in Fig. 1.

Table 1 shows the timetable for ground and aircraft measurements during the SIJAQ campaign and the daily mean surface meteorological conditions observed at ASOS, including cloud cover (%), weather conditions, temperature (°C), and relative humidity (%). The daily weather conditions were classified as mist, haze, clear, and rainy. During the campaign, a total of 23 clear days, 7 rainy days, 9 mist days, and 6 haze days were recorded. The mist days were observed on the 26–27 October, 4–6 November, and 18–21 November 2021. Mist was mostly associated with a relative humidity of 63–85%, and haze events often occurred on the same days, such as on the 25 and 27 October and 18–21 November. We followed the operational definitions for these conditions used by the KMA; haze refers to conditions with daily mean relative humidity (RH) $< 75\%$ and daily mean visibility (VIS) between 1 and 10 km, mist refers to conditions with daily mean RH of $\geq 75\%$ and daily mean VIS between 1 and 10 km, and fog refers to days with daily mean RH $\geq 75\%$ and daily mean VIS <1 km.

Aircraft measurements were carried out 16 times using the Radio Frequency Airborne, Interception, Moving Target Indicator, and Multi-function System–30 (RF_AIMMS-30) (flights RF01–16; flight RF01 was a test flight) and 11 times using the GCAS instrument (flights #01–11)

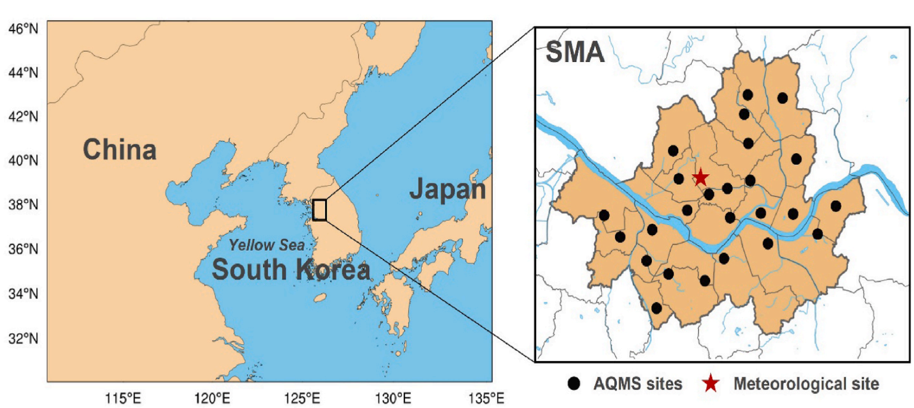

Fig. 1. Locations of air quality monitoring (AQM) sites and a meteorological site in the Seoul metropolitan area (SMA) in South Korea. The meteorological and chemical measurements were used to interpret the multi-perspective observations collected across the SMA during the SIJAQ campaign from 10 October to 25 November 2021.

Table 1
Ground and aircraft measurements and daily meteorological conditions during the SIJAQ campaign (10 Oct–25 Nov 2021).

Date (2021)	(Aircraft Measurement) (*hhmm-hhmm*) (LST)		(Ground Measurement) (*hhmm-hhmm*) (LST)		(Weather Condition)			
	RF_AIMMS-30	RF_GCAS	MAX-DOAS	CAR-DOAS	CC (%)	Weather (mm)	T (°C)	RH (%)
18 Oct.	RF01:Test Flight				66	Rain(0.8)	9.6	60.4
19 Oct.	RF02:0854–1029		0741–1655		40	Rain(0.7)	10.9	72.8
20 Oct.			0720–1717	1051–1802	3		9.5	64.9
21 Oct.			0718–1716		33		9.8	64.1
22 Oct.			0719–1717	1009–1804	8		10.8	58.4
23 Oct.	RF03:0829–1110 RF04:1325–1628		0720–1719		3		11.4	57.3
24 Oct.	RF05:0840–1132 RF06:1346–1643		0721–1713		3		11.4	63.1
25 Oct.			0720–1718		8		11.7	64.5
26 Oct.	RF07:1333–1655		0723–1709	1442–1455	36	Mist	13.0	74.5
27 Oct.	RF08:0813–1049		0723–1710	0905–1758	25	Mist	13.4	63.4
28 Oct.			0724–1713	1020–1734	0		12.7	54.6
29 Oct.			0725–1716		46		14.6	55.9
30 Oct.			0726–1717		61		13.8	62.4
31 Oct.			0728–1715		38	Rain(0.7)	14.1	73.3
1 Nov.	RF09:0809–1035		0729–1703	1009–1650	30		12.9	77.3
2 Nov.			0729–1702	0900–1701	40		11.5	76.6
3 Nov.		#01:1122–1555	0730–1701	0905–1414	30		12.1	71.1
4 Nov.	RF10:0828–1135 RF11:1317–1442		0733–1707		24	Mist, Haze	12.1	80.4
5 Nov.		#02:0925–1106 #03:1307–1626	0733–1705	0900–1624	6	Mist, Haze	13.0	68.5
6 Nov.	RF13:0829–1108 RF14:1329–1537		0735–1706		13	Mist	14.1	61.1
7 Nov.			0735–1707		70		15.3	57.5
8 Nov.			0749–1654		99	Rain(4.3)	8.6	82.1
9 Nov.			0749–1703		81	Rain(0.3)	4.9	80.3
10 Nov.			0744–1701		74	Rain(0.1)	4.2	73.4
11 Nov.			0741–1701		30		5.3	60.6
12 Nov.		#04:0919–1139 #05:1248–1520	0741–1658	0902–1541	13		4.5	55.4
13 Nov.	RF15:0905–1206		0743–1702		45		7.3	66.1
14 Nov.	RF16:1225–1510	#06:1127–1545	0746–1701		34		11.3	69.8
15 Nov.			0745–1658		36		10.1	71.3
16 Nov.		#07:0946–1228 #08:1407–1646	0745–1650	0914–1341	0		8.5	65.5
17 Nov.		#09:0928–1215 #10:1316–1600	0746–1649	0824–1620	35		7.5	64.1
18 Nov.					75	Mist, Haze	11.9	70.8
19 Nov.		#11:1143–1539	0750–1657		65	Mist, Haze	12.9	84.8
20 Nov.			0756–1646		33	Mist, Haze	10.4	77.0
21 Nov.			0752–1649		89	Mist, Haze	10.4	74.4
22 Nov.			0752–1645		33	Rain(3.6)	2.7	61.8
23 Nov.			0755–1647		29		−0.6	60.9
24 Nov.					39		4.1	64.3
25 Nov.					19		5.7	55.0

RF_AIMMS-30: Aircraft measurements with an ambient ion monitor (AIM, URG 9000D).
RF_GCAS: Flight with GCAS instrument.
CC: Cloud Cover (%).

(Table 1). Ground measurements were taken 35 times using the Max-DOAS and 12 times using the CAR-DOAS. The average cloud cover during GCAS-based aircraft measurements was 26.1%, and all GCAS flights (except for flight #11) were taken during a cloud cover of 35%.

Fig. 2 shows the temporal variation in $PM_{2.5}$, PM_{10} concentrations, and ratio of $PM_{2.5}$ to PM_{10} (=$PM_{2.5}/PM_{10}$) observed at the AQM sites (Fig. 1). During the campaign, the mean $PM_{2.5}$ and PM_{10} concentrations were 21.9 ± 13.5 μg m^{-3} and 35.7 ± 18.2 μg m^{-3}, respectively, and their variations showed similar patterns (Fig. 2). The ratio of $PM_{2.5}$ to PM_{10} was in the range of 0.4–0.6 (with an average of 0.52) during the campaign, suggesting that there was minimal influence from natural emissions such as Asian dust. However, the long-term mean PM_{10} concentration increased slightly during the day, while the $PM_{2.5}$ concentration decreased slightly during the day throughout the campaign. As a result, the ratio of $PM_{2.5}$ to PM_{10} concentrations (average = 0.55) decreased during the day (Fig. 2).

Three $PM_{2.5}$ peaks were observed, with the first peak occurring from the 4 to 6 November and the second peak occurring from the 19 to 21 November (Fig. 2). The daily variation in $PM_{2.5}$ concentration on the 4–6 and 19–21 November exceeded the daily environmental standard of 35 μg m^{-3}, and GCAS flight #11 and ground measurements using the Max-DOAS were carried out during these two peaks. On 26–27 October, the third $PM_{2.5}$ peak was observed, with a 2-day mean $PM_{2.5}$ concentration of 22.5 μg m^{-3}. During this period, the flights RF07–08, GCAS flights #08–09, and ground measurements using both the Max-DOAS and the Car-DOAS were carried out.

3. Meteorological features during the campaign

3.1. Climatological features: La Niña events in 2021

The year 2021 was cooler than recent years in the northern hemisphere due to the influence of moderate La Niña events (WMO, 2022). La Niña has a temporary cooling effect on the global mean temperature, and the year 2021 was around 0.22 °C–0.29 °C warmer than 2011, which was the strongest La Niña year. In contrast to the El Niño year of

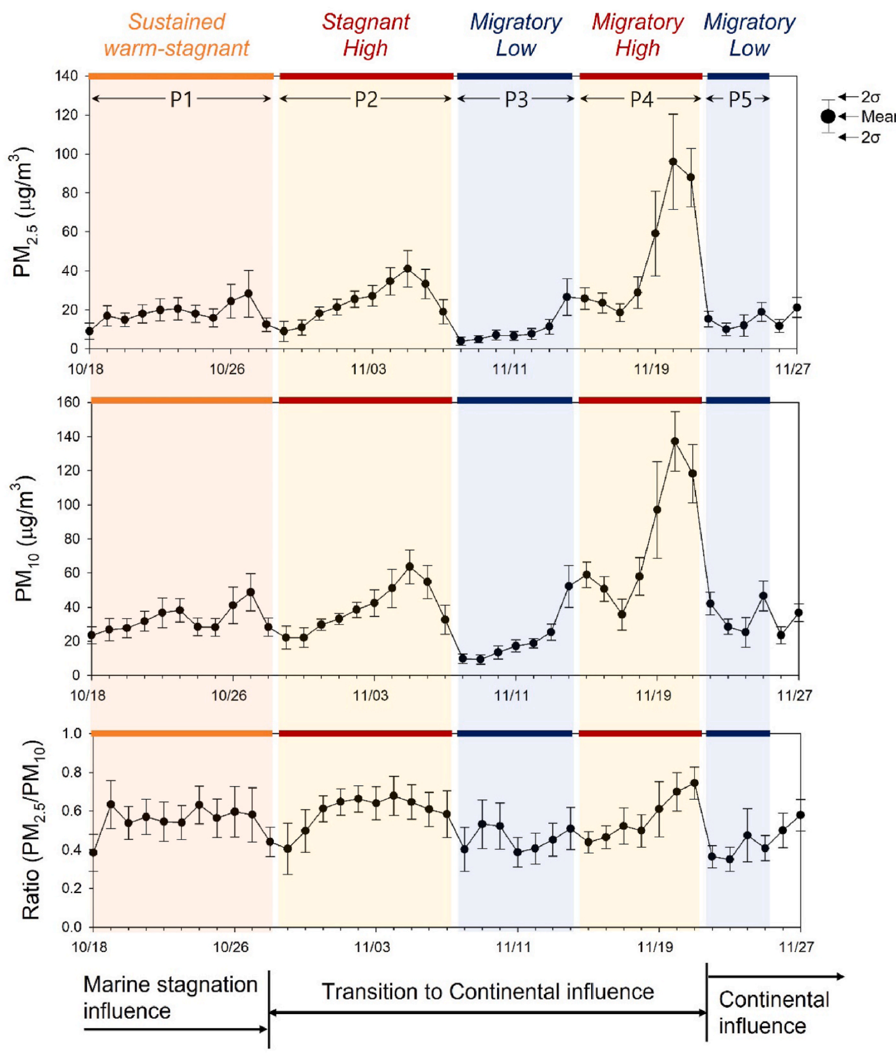

Fig. 2. Time series of daily mean $PM_{2.5}$ and PM_{10} concentrations, and ratio of $PM_{2.5}$ to PM_{10} (=$PM_{2.5}/PM_{10}$) observed at AQM sites over the SMA. P1–P5 represent the five synoptic periods during the SIJAQ campaign (10 October to 25 November 2021). Here, σ denotes one standard deviation.

2016, the weak La Niña year 2021 remains the warmest year on record according to most decadal datasets (WMO, 2022). During that year, the climate on the Korean Peninsula during the summer season was hot and humid due to the North Pacific high-pressure system and cold and dry during the winter season due to the Siberian high-pressure system (KMA, 2022). The Korean Peninsula was affected by a very strong La Niña during the year and was governed by an abnormally expanded North Pacific high that stretched to 40°N latitude in the Western Pacific region (Fig. 3). The summer monsoonal front was located in the 20–30°N latitude throughout the SIJAQ campaign, and the Korean Peninsula experienced warmer and drier weather compared to previous climatological records.

Air temperature and precipitation in 2021 were compared to the climatological records of the 30-year period from 1981 to 2010. The SIJAQ campaign period was much warmer and drier compared to previous climatological records. The mean air temperature during the SIJAQ campaign was 22.7 °C, which is higher than the mean of climatological records (20.1 °C; KMA). The daily maximum air temperature during the SIJAQ campaign exceeded the mean of climatological records. Very little precipitation (less than 1 mm/day during most rainy days) was recorded during the campaign, except for the 8 November, which had a precipitation of 4.3 mm/day. The mean temperature recorded at the ASOS sites in the SMA was 7–8 °C (Table 1).

3.2. *Synoptic characteristics*

During the SIJAQ campaign, nine migratory or stagnant anticyclones and three cyclones passed over the Korean Peninsula. We traced the pathways and origins of these anticyclones and cyclones that affect air quality. Daily weather charts were analyzed to provide anticyclone pathways throughout the campaign. The synoptic features were classified into five periods (P1–P5) based on traced pathways. The categories are illustrated as a time sequence in Fig. 2 and their main features are described below.

P1 corresponds to sustained marine stagnation, P2 to a transitional stagnant high, P3 to a continental migratory low, P4 to a continental migratory high, and P5 to a continental migratory low.

3.2.1. *P1: Sustained marine stagnation (10–28 Oct 2021)*

During P1, the Korean Peninsula experienced sustained marine stagnation, which was caused by a persistent influence of the North Pacific oceanic high-pressure system that remained over the region for a considerable period, as shown in the weather charts for 850 and 500 hPa on 13 October (Fig. 3). As a result, temperatures were higher than in the past 30 years, due to the influence of the southern marine area. Throughout P1, a stagnant high-pressure system, which originated from a marine high-pressure system (e.g., 850 hPa in Fig. 2), was present. Overall, $PM_{2.5}$ concentrations were not elevated during this period,

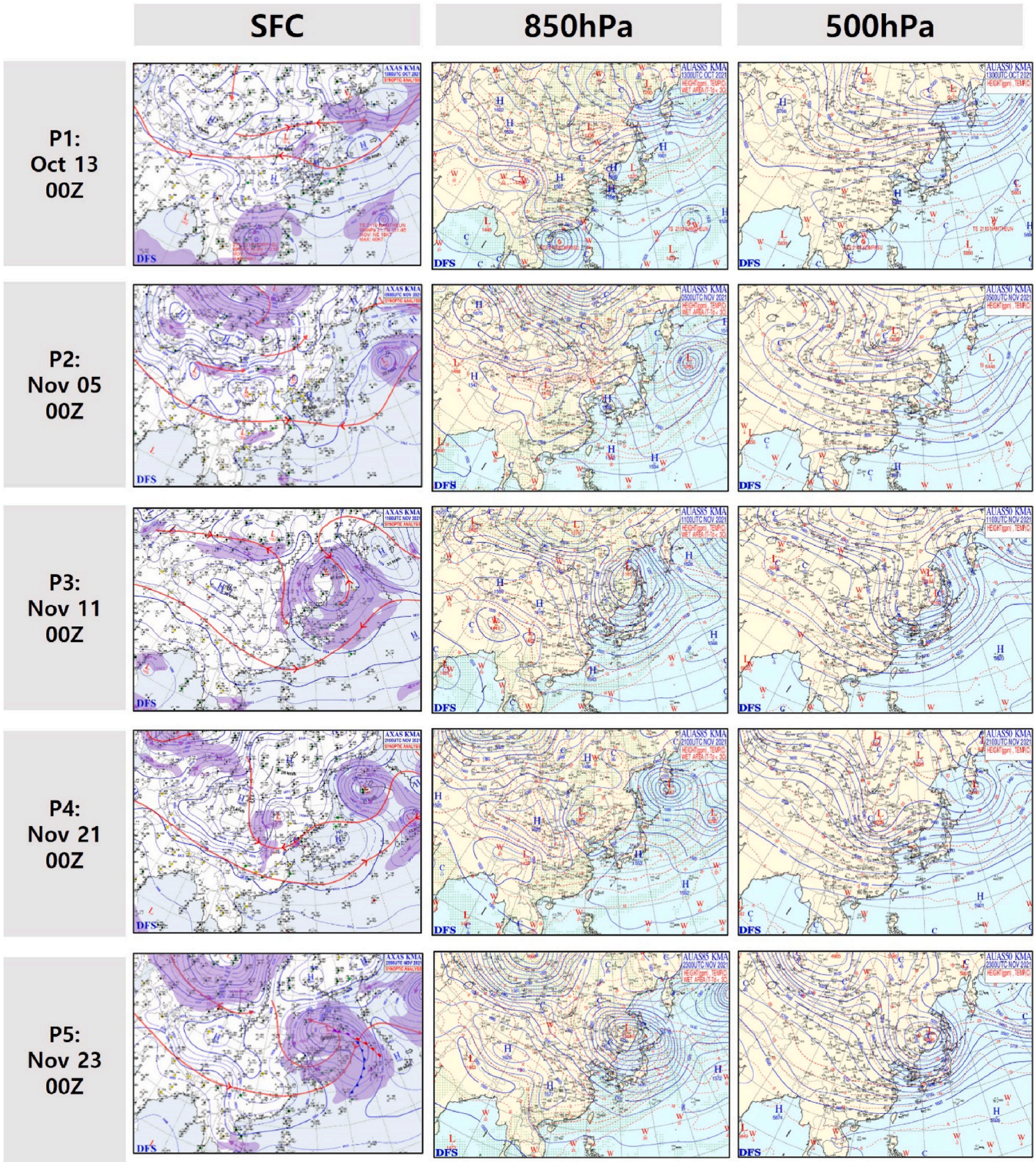

Fig. 3. Weather charts of surface (left), 850 hPa (middle), and 500 hPa (right) geopotential levels at 0900 LST (0000 UTC) on 13 October (first row), 5 November (second row), 11 November (third row), 21 November (fourth row), and 23 November (fifth row), 2021. Charts show representative days for the five synoptic periods (P1–P5) during the SIJAQ campaign (http://data.kma.go.kr). Bold red lines indicate an upper-level jet stream.

except for the stagnation day (27 October; Fig. 2), mainly due to the influence of the clean marine atmosphere.

3.2.2. P2: Transitional stagnant high (29 Oct–07 Nov 2021)

During P2, there was a transitional period from the hot and humid North Pacific high in summer to the cold and dry continental high in winter. Stagnant high pressures of marine origin were mixed with continental migratory pressures, resulting in clear and dry days and $PM_{2.5}$ peaks, such as on the 5–6 November during the stagnation of high pressure over northeastern Asia. On the 5 November, weak wind speeds of 850 hPa (=2.1 m/s) and weak easterly surface wind conditions lead to higher $PM_{2.5}$ concentrations over the SMA (Fig. 3). These meteorological conditions provide the ideal basis to understand how pollutants originating from local emission accumulation can be controlled over the SMA region.

3.2.3. P3: Continental migratory low (08–14 Nov 2021)

Continental migratory low-pressure systems prevailed during P3. Temperatures dropped sharply, as indicated in Table 1, and high upper-level wind speeds, such as the geostrophic wind speed at 850 hPa geopotential height, exceeded 15 m/s for 5 consecutive days (8–12 November 2021). In addition, 3 consecutive days of precipitation were observed (8–10 November 2021) (Table 1). These phenomena might be attributed to the significant impact of the cyclone of continental air flow, and as a result, lower $PM_{2.5}$ levels were observed throughout the P2 period over the entire SMA (Fig. 2).

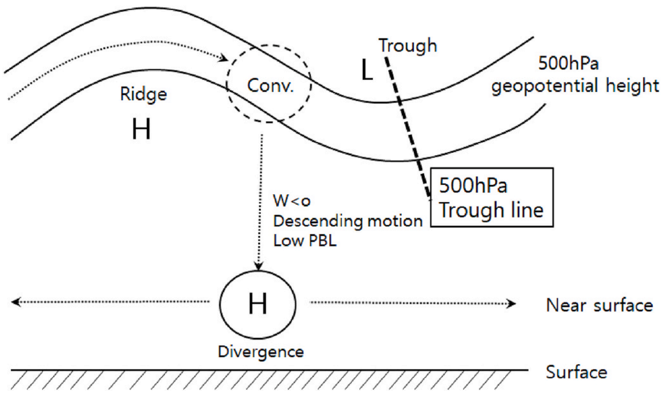

Fig. 4. A schematic diagram of upper-level sinusoidal isobars superimposed on lower-level circular isobars and the resulting vertical motion.

3.2.4. *P4: Continental migratory high (15–21 Nov 2021)*

After the cyclone passed through the Korean Peninsula, a weak northwesterly influence was observed in the upper atmosphere at 500 and 850 hPa, followed by slowly moving or nearly stagnating high pressure at 850 hPa over the Korean Peninsula. The geostrophic wind speed at 850 hPa was 7.3 m/s on 20 November, and surface winds were weak. In addition, on two previous days (18–19 November), stronger geostrophic wind speeds at 850 hPa of 10 m/s and higher were observed, which resulted in the highest $PM_{2.5}$ levels observed during the entire SIJAQ campaign. These high levels likely resulted from the combined influence of both external emission sources and internal emissions. On 20 November, the highest level of $PM_{2.5}$ in the SMA was 83.4 μg m^{-3} (Fig. 1). These observations provide a good basis to investigate the impact of transboundary transport processes of air pollutants on $PM_{2.5}$ levels over the SMA during the SIJAQ campaign. A comprehensive analysis of the impact of higher $PM_{2.5}$ concentrations could be achieved by tracing the fate of pre-pollution and combining aircraft measurements and comprehensive modeling studies for separate periods, specifically before (18–19 November), during (20 November), and after (21–22 November) the transboundary transport process along the latitude directions at 850 hPa altitudes. This is discussed further in section 3.4.

3.2.5. *P5: Continental migratory low (22–25 Nov 2021)*

On 22 November, a continental cyclone emerged, resulting in strong winds in both the upper and surface atmospheres. The strong geostrophic wind speed of 26 m/s at 850 hPa geopotential height on the 22 November was the highest speed observed during the entire SIJAQ campaign. As a result, significantly low $PM_{2.5}$ levels with daily concentrations of less than 15 μg m^{-3} were observed over the entire SMA (Fig. 2).

3.3. *Synoptic conditions for high $PM_{2.5}$ cases*

Although this is a case study conducted within a restricted campaign period, we specifically focus on the synoptic vertical motions in association with high $PM_{2.5}$ accumulations. The synoptic descending or ascending dynamics are particularly relevant due to two key factors. Firstly, when surface-level PM concentrations are influenced by transboundary airflow, synoptic vertical phenomena become closely associated with synoptic descending motions from the mid-troposphere into the mid-lower atmosphere, allowing the $PM_{2.5}$-laden air to intrude

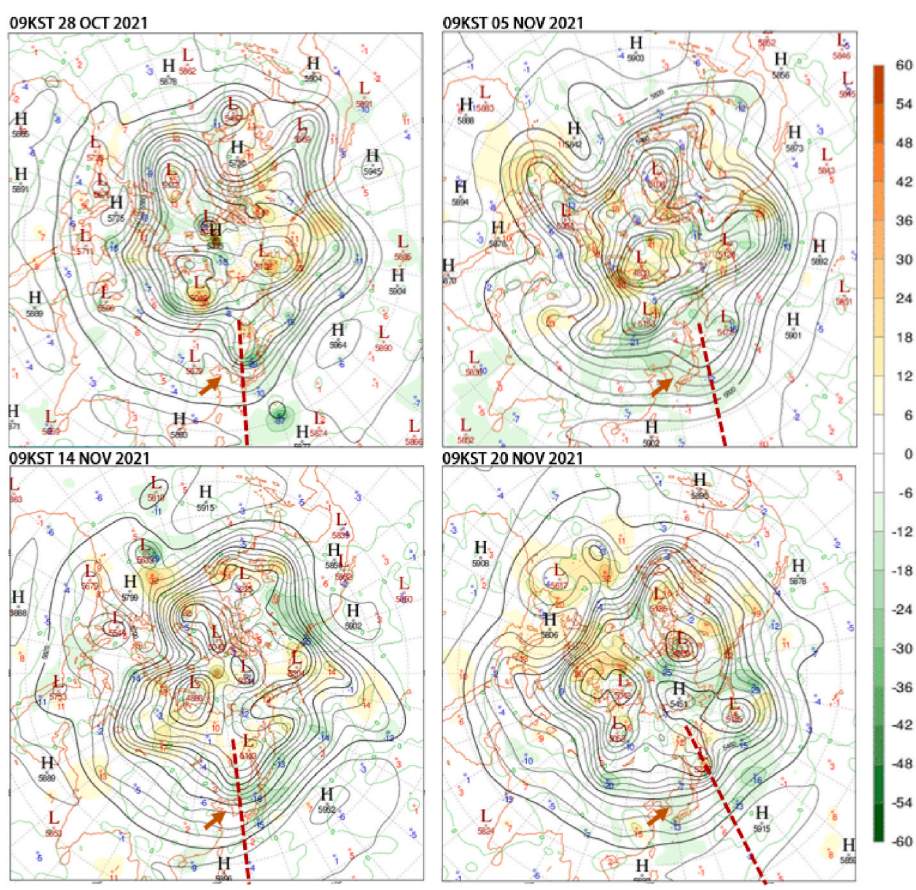

Fig. 5. Geopotential height fields of 500 hPa over the northern hemisphere. Arrow denotes location of Korean Peninsula, and dashed line indicates the ridgeline around the Korean Peninsula.

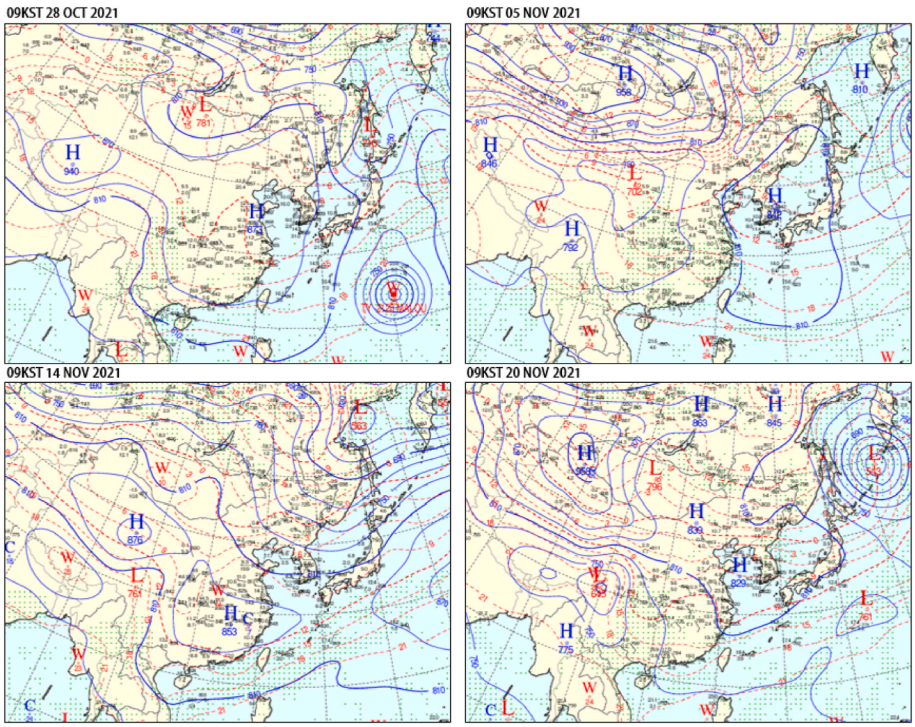

Fig. 6. Weather charts of near-surface (925 hPa) geopotential level at 0900 LST (0000 UTC) on 28 October (top-left), 5 November (top-right), 14 November (bottom-left), and 19 November (bottom-right), 2021. Charts show the highest $PM_{2.5}$ days for the four synoptic periods (P1–P4) during the SIJAQ campaign (http://data.kma.go.kr).

closer to the surface in cases of transboundary transport case. Secondly, in cases of local accumulation, synoptic descending motion can hinder the development of the planetary boundary layer (PBL) height, resulting in progressive PM accumulation within the lower PBL; thus facilitating the formation of severe PM pollution. Therefore, it is crucial to investigate the dynamic vertical motions under various synoptic conditions when interpreting surface $PM_{2.5}$ levels.

Fig. 4 depicts a plan view of upper-level isobars (i.e., 500 hPa geopotential height) superimposed on the resulting vertical distribution of convergence and divergence. As shown in Fig. 4, convergence occurs to the west of the trough line at the mid-to upper-troposphere such as at 500 hPa geopotential level, while divergence takes place ahead of the trough line (Hess, 1959). On the other hand, at the surface level, a distinct pattern of near-surface divergence is observed, coinciding with descending motions originating from the mid- or upper-troposphere. This phenomenon is especially pronounced in cases of high $PM_{2.5}$ concentrations, wherein a high-pressure system is present to the east of the trough line at the 500 hPa geopotential level.

In our study, upon examination of Fig. 4, a significant qualitative agreement was observed during the high $PM_{2.5}$ episodes of the SIJAC campaign. Fig. 5 illustrates the 500 hPa geopotential levels over the northern hemisphere on higher $PM_{2.5}$ days: 28 October, 5, 14 and 20 November 2021, which are the days with the highest observed $PM_{2.5}$ concentrations in each of the four categorized periods (P1–P4). The 500 hPa geopotential level at 0900LST on these chosen days shows the sinusoidal wave patterns of air motion at 5–6 km above sea level pressure, well characterized by undulating and meandering upper-level airflow throughout the campaign period. However, it is noteworthy that a large transition pattern from ridge to trough covers much of central China, while the troughs are consistently located to the east of the Korean Peninsula on all four chosen high $PM_{2.5}$ episodic days, exerting influence on the high surface $PM_{2.5}$ concentrations by inducing vertical descending motions (see Fig. 5).

In the near-surface atmosphere (i.e., 925 hPa geopotential level), three high $PM_{2.5}$ days: 28 October, 5, and 20 November exhibit high pressure systems positioned near the surface (Fig. 6), which align well with the left wing of the trough lines as shown in Fig. 5. On 14 November, the surface high pressure was not observed over the Korean Peninsula but was instead located in close proximity to southern China and the Yellow Sea. However, no upward motion was detected. Although the interplay of a few simple meteorological factors can provide an interpretation compatible with the observed $PM_{2.5}$, it is important to note that these vertical interpretations are qualitative rather than quantitative. This is primarily due to the continuous eastward movement of weather systems, which presents challenges in providing quantitative assessments.

Other meteorological factors, such as humidity and stability, also play a significant role. Many previous studies have revealed a strong correlation between $PM_{2.5}$ levels and atmospheric stability. This is because the presence of a high $PM_{2.5}$ layer leads to surface cooling through scattering and absorption, while simultaneously heating the atmosphere through solar radiation absorption. This process enhances air static stability, resulting in $PM_{2.5}$ accumulations in the lower troposphere. Unfavorable meteorological conditions, such as shallow PBL, low wind speeds, and high relative humidity, also exacerbate further the $PM_{2.5}$ levels.

In summary, despite the limited duration of our campaign period, our investigation highlights the significance of meteorological vertical motion and the vertical pressure structure up to 500 hPa in characterizing the transboundary transport process of high $PM_{2.5}$ on a regional scale; however, further analysis, including model simulations for recent years, is necessary to comprehensively evaluate the meteorological factors contributing to high $PM_{2.5}$ episodes over SMA.

3.4. *Transboundary transport vs. local accumulation*

In previous studies, synoptic meteorological parameters have been used to diagnose air pollution over source regions (Dobbins, 1979; Sanchez et al., 1990; Davis and Gay, 1993). To distinguish between local accumulation-driven (LAD) case and transboundary transport (TBT)

Table 2
Selected synoptic meteorological variables over the SMA during the SIJAQ campaign. The variables used were calculated at the 850 hPa geopotential level.

Date (2021)	Geosptrophic wind speed (m s^{-1})	Vorticity (* 10^{-5} s^{-1})	Vorticity advection (* 10^{-9} s^{-1})	RH_{eff} (%)	S (°C)
18 Oct.	3.8	−10.1	−1.5	31.7	3.1
19 Oct.	7.8	3.3	−19.5	43.3	1.2
20 Oct.	1.9	−3.2	1.4	49.1	0.5
21 Oct.	3.3	6.9	0.3	52.4	1.7
22 Oct.	2.6	−0.6	0.5	48.9	0.8
23 Oct.	3.1	−2.0	−0.8	47.4	1.7
24 Oct.	5.2	0.3	−0.2	46.6	2.6
25 Oct.	3.7	−1.2	4.7	48.0	1.7
26 Oct.	4.6	−7.3	3.0	52.5	4.3
27 Oct.	13.6	3.7	−3.3	55.3	2.3
28 Oct.	11.7	2.2	−8.1	51.3	6.8
29 Oct.	1.4	−9.1	1.4	44.2	2.6
30 Oct.	3.7	−3.5	1.8	41.2	1.3
31 Oct.	4.9	−2.5	−7.8	46.7	2.6
1 Nov.	4.6	−6.3	1.5	54.4	1.5
2 Nov.	1.3	−3.8	3.3	60.3	0.8
3 Nov.	2.3	3.7	3.1	59.5	1.3
4 Nov.	6.1	−3.0	3.4	58.9	1.9
5 Nov.	2.1	−7.7	1.5	59.2	1.4
6 Nov.	3.6	−5.5	−1.6	56.3	2.5
7 Nov.	6.1	−0.6	−11.7	51.3	3.2
8 Nov.	23.2	2.6	−38.1	53.6	−0.8
9 Nov.	25.5	6.3	−59.1	56.4	−0.9
10 Nov.	20.0	1.2	−26.7	59.3	−2.3
11 Nov.	19.4	7.2	−36.0	50.7	−0.3
12 Nov.	15.8	−7.1	−22.4	43.4	−0.6
13 Nov.	8.4	−5.8	−17.8	42.4	−2.6
14 Nov.	12.4	0.2	−0.4	47.9	−3.3
15 Nov.	8.5	−0.5	3.0	55.9	−2.2
16 Nov.	8.1	−0.8	5.0	58.8	−0.7
17 Nov.	8.7	1.6	−3.3	58.5	4.0
18 Nov.	13.3	−0.2	−44.1	51.1	−2.1
19 Nov.	13.0	−4.3	−22.1	54.4	−0.6
20 Nov.	7.3	1.9	6.7	57.1	4.9
21 Nov.	5.4	2.0	−10.0	56.6	−1.4
22 Nov.	26.0	4.2	−42.4	44.5	−2.9
23 Nov.	16.7	3.3	−98.5	38.3	−2.2
24 Nov.	18.1	−3.5	−67.9	36.2	−2.1
25 Nov.	17.9	3.7	−3.1	41.4	−1.0

*The definitions for the RH_{eff} and S are provided in the main text.

dominant processes, various synoptic variables have been employed. Jo and Kim (2013) proposed 17 synoptic variables to distinguish between LAD and TBT processes in northeastern Asia and reported classification accuracies of 93.2%, 87.8%, 85.4%, and 84.4%, respectively. Of these variables, we selected five: geostrophic wind speed, vorticity, vorticity advection at the 850 hPa geopotential level, vertical stability index, and effective humidity (RH_{eff}), which we used to diagnose the meteorological characteristics for P1– P5 and to distinguish periods into TBT and LAD processes (Jo and Kim, 2013).

We used National Centers for Environmental Prediction Final reanalysis data with a resolution of 1° × 1° to calculate dynamic variables, including geostrophic wind speed, vorticity, and vorticity advection from the nearest grid to the SMA. The east-west and south-north components of wind and geostrophic wind vectors are represented by (u, v) and (ug, vg), respectively. We used effective humidity, $RH_{eff} = 0.3\ (RH_{d\text{-}0} + 0.7\ RH_{d\text{-}1} + 0.72\ RH_{d\text{-}2})$, as a measure of humidity, where RH is relative humidity and d-*i* is the *i*th day prior to the indicated day (Jo and Kim, 2013; Lee and Park, 1997). The vertical stability index of the lower atmosphere represents the temperature lapse rate between geopotential height fields of 1000 hPa and 850 hPa and is defined as T_{850}–T_{1000}, where T_{1000} and T_{850} are the temperatures at 1000 hPa and 850 hPa, respectively.

Table 2 presents the synoptic variables in the SMA during the campaign period. Vorticity is the most crucial variable indicating high air pollutants, and combining geostrophic wind speed with vorticity helps distinguish between two types of days (Kim et al., 2012; Jo and Kim, 2013). TBT-dominated elevated $PM_{2.5}$ days under the process showed lower geostrophic wind speed, negative vorticity, higher vorticity advection, and unstable (or neutral) lower atmospheric stability. By contrast, LAD-dominated elevated $PM_{2.5}$ days showed higher geostrophic wind speed, negative vorticity, lower vorticity advection, and stable lower atmospheric stability. In addition, the humidity index, RH_{eff}, tended to be drier under the TBT process than under the LAD process (Jo and Kim, 2013). Table 2 lists five synoptic variables selected for the entire campaign period, and the P2 and P4 periods contrasted well with the P3 and P5 periods in terms of both geostrophic wind speed and vorticity. Specifically, P3 and P5 exhibited strong geostrophic wind speeds of 17.8 ± 6.0 m/s (P3) and 19.7 ± 4.3 m/s (P5) and positive vorticity. On the other hand, the P2 period had a significantly lower geostrophic wind speed of 4.4 ± 3.2 m/s with negative vorticity of −2.4 ± 4.2 × 10^{-5} s^{-1}. The P4 period had a negative vorticity and a geostrophic wind speed of 9.2 ± 2.9 m/s, indicating relatively stronger geostrophic wind speed than that observed during P2. However, negative vorticity advection, a positive stability index, and relatively drier RH_{eff} were observed for both P2 and P4 periods. These results suggest that weak ventilation effects and lower transport processes in the stable atmosphere prevailed during the P2 period, whereas some ventilation effects likely occurred during the P4 period due to the relatively stronger geostrophic wind speed in the 850 hPa level, indicating that P2 was LAD-dominated and P4 was TBT-dominated.

As a case study, we analyzed the 2 days during which two high $PM_{2.5}$ peaks occurred in depth, specifically the 5 November (Case 1, LAD-driven) in the P2 period and the 19 November (Case 2, TBT-induced) in the P4 period (Fig. 2). Wind fields with pressure patterns at the surface and 850 hPa levels for the two cases over the Korean Peninsula are presented in Fig. 7. Case 1 (5 November) showed a weak geostrophic wind speed of 2.1 m/s and weak easterly surface wind conditions throughout the day (Fig. 7a). These meteorological conditions imply that Case 1 was affected by a local-emissions-driven $PM_{2.5}$ peak without extensive external transport from outside. In comparison, Case 2 (19 November) showed prevailing northeasterly winds with a rather strong geostrophic wind speed of 7.3 m/s at the 850 hPa geopotential level (Fig, 7d), which implies a high level of influx at the 850 hPa level from China through the TBT process, which accumulated over the SMA.

Both cases are clearly distinguishable in Fig. 8, which shows the observed vertical structure of wind vectors at the SMA. The two yellow boxes denote Case 1 and Case 2. In Case 1, weak wind vectors from the surface to the upper atmosphere over the SMA are present. Importantly, wind speeds were very weak on the 2 previous days (3–4 November). On the following 2 days (6–7 November), the wind direction gradually changed to the easterlies (blue arrows in Fig. 8). These easterlies likely induced strong convergence zones over the SMA with little ventilation effect until the following days, representing a typical LAD-dominant case in which pollutants are mostly locally emitted and accumulated during the day.

By contrast, Case 2 showed weak surface but relatively stronger upper wind speeds on 19 November compared to 5 November. Interestingly, stronger horizontal westerlies and vertically weak descending wind vectors were present on the previous days (18–19 November) at the same time, and weak wind speeds from the surface to the upper atmosphere were observed on 20 November. Based on this, the TBT process can be divided into three phases: the pre-transportation (first) phase, the transportation (second) phase, and the post-transportation (third) phase along latitudinal and vertical directions.

The first stage (18–19 November) was associated with the transport process of pre-pollution under strong horizontal wind speeds, particularly at higher altitudes (i.e., 850 hPa altitude) (Fig. 8). During the second stage (20 November), horizontal weak wind speeds were dominant, but vertically descending motions or convective processes started to occur, resulting in a vertical mixing effect replenishing or merging with the locally accumulated pollution concentrations at the ground

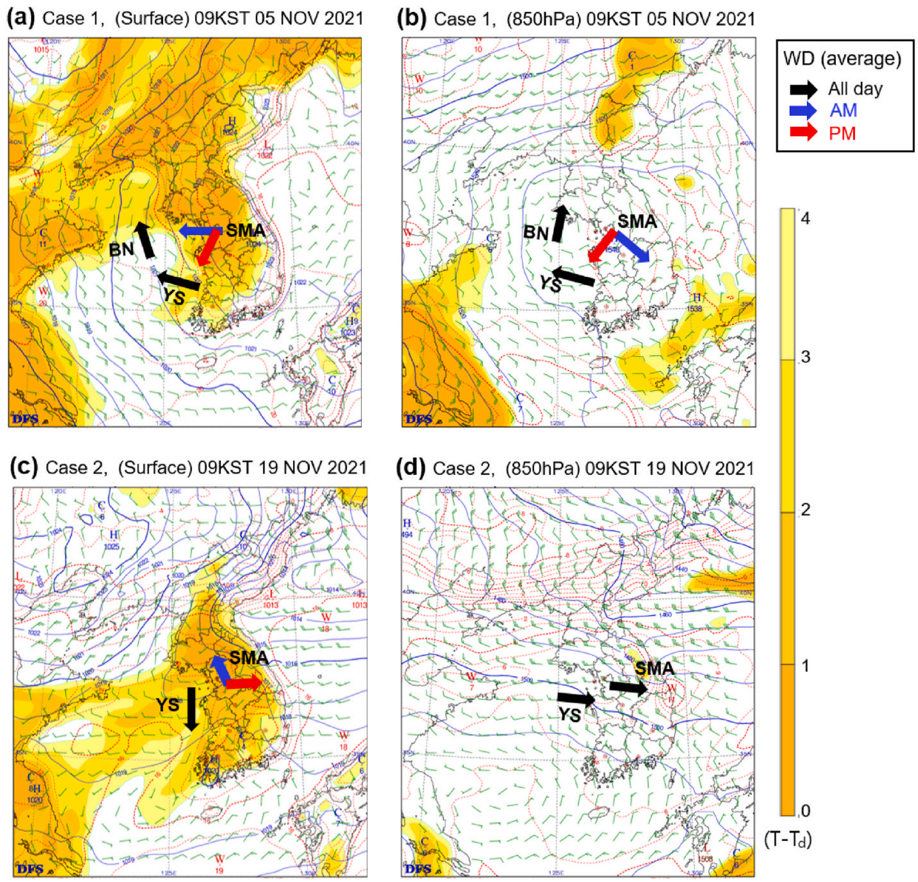

Fig. 7. Weather charts of surface (left) and 850 hPa geopotential level (right) at 0900 LST (0000 UTC) on 5 November (a)(b), and 19 November (c)(d), 2021 (http://data.kma.go.kr). Arrows indicate the mean wind vectors observed at the SMA, Yellow Sea (YS), and Baengnyeong Island (BN).

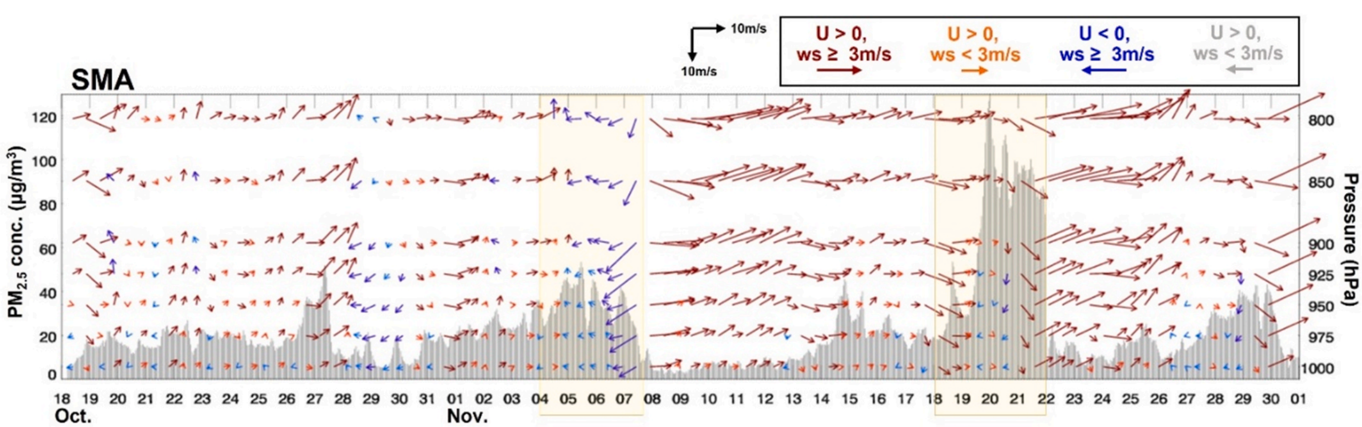

Fig. 8. Vertical profiles of wind vectors observed in the SMA during the SIJAQ campaign. The two yellow boxes denote the two case study periods (Case 1 and 2).

level. This resulted in the highest pollutant concentrations. Further research is required to determine if vertical advection or turbulent-induced convective processes are more important in vertical mixing. During the third stage (21–22 November), the high-pollution area driven by external transport and local accumulation gradually dissipated or was transported, ventilating the high pollution concentrations.

Our interpretation of the two processes, LAD and TBT, is based purely on meteorological factors, and to draw general conclusions, a detailed and in-depth analysis that involves comprehensive modeling and ground and aircraft measurements analysis is required, in particular regarding the vertical mechanisms of transport and accumulation processes of $PM_{2.5}$ pollutants at an altitude of 1–1.5 km around the Yellow Sea area. More detailed numerical and aircraft observational studies on the SIJAQ campaign are featured in this issue.

4. Summary

To investigate the meteorological factors collected during the SIJAQ field campaign from 10 October to 25 November 2021, we present an overview of synoptic meteorological characteristics. We also analyzed the meteorological features in association with $PM_{2.5}$ levels over the SMA. We traced cyclone and anticyclone pathways through weather charts and separated the SIJAQ campaign into five periods (P1–P5). Then we analyzed the synoptic features of each period.

Furthermore, we thoroughly discussed two types of $PM_{2.5}$ peak concentration processes, local accumulation and transboundary transport process. We took the dates 5 and 20 November as case studies, as they were representative of each process. For each case study, five synoptic meteorological variables that represent synoptic characteristics were analyzed. While we identified meteorological characteristics for each process, our analysis was based purely on observed meteorological evidence. Therefore, a multi-analysis of both physical and chemical air quality conditions based on aircraft and ground measurements obtained during the SIJAQ campaign is required to draw general conclusions, which is featured in this issue. Nevertheless, our meteorological interpretation can be useful to identify the causes of high $PM_{2.5}$ episodes over the SMA.

CRediT authorship contribution statement

Cheol-Hee Kim: Supervision, Conceptualization, Writing – original draft. **Hyun-Young Jo:** Data curation, Visualization. **Yu-Jin Jo:** Methodology, Formal analysis. **Hyo-Jung Lee:** Methodology, Formal analysis. **Jong-Min Kim:** Data curation, Visualization. **Na-Mi Lee:** Data curation, Visualization. **So-Yeon Jeong:** Data curation, Visualization. **Seung-Hee Baek:** Data curation, Visualization. **Min-Jun Park:** Data curation, Visualization. **Lim-Seok Chang:** Conceptualization, Methodology, Validation. **Jong-Jae Lee:** Data curation, Visualization. **Chang-Keun Song:** Conceptualization, Investigation.

Declaration of competing interest

The authors declare that they have no known competing financial interests or personal relationships that could have appeared to influence the work reported in this paper.

Data availability

Data will be made available on request.

Acknowledgments

This work was supported by a grant from the National Institute of Environmental Research (NIER), funded by the Ministry of Environment (ME) of the Republic of Korea (NIER-2021-04-02-086 and NIER-2022-04-02-037), and also partially supported by the Basic Science Research Program through the National Research Foundation of Korea (NRF) funded by the Ministry of Education (2020R1I1A2075417 and 2020R1A6A1A03044834).

References

Chang, L.-S., Kim, D., Hong, H., Kim, D.-R., Yu, J.-A., Lee, K., Lee, H., Kim, D., Hong, J., Jo, H.-Y., Kim, C.-H., 2022. Evaluation of correlated Pandora column NO2 and in situ surface NO2 measurements during GMAP campaign. Atmos. Chem. Phys. 22, 10703–10720.

Crawford, J.H., Ahn, J.-Y., Al-Saadi, J., Chang, L., Emmons, L.K., Kim, J., Lee, G., Park, J.-H., Park, R.J., Woo, J.H., Song, C.-K., Hong, J.-H., Hong, Y.-D., Lefer, B.L., Lee, M., Lee, T., Kim, S., Min, K.-E., Yum, S.S., Shin, H.J., Kim, Y.-W., Choi, J.-S., Park, J.-S., Szykman, J.J., Long, R.W., Jordan, C.E., Simpson, I.J., Fried, A., Dibb, J. E., Cho, S.Y., Kim, Y.P., 2021. The Korea–United States air quality (KORUS-AQ) field study. Elem. Sci. Anth. 9 (1), 00163.

Davis, R.E., Gay, D.A., 1993. A synoptic climatological analysis of air quality in the Grand Canyon National Park. Atmos. Environ. 27 (5), 713–727.

Dobbins, R.A., 1979. Atmospheric Motion and Air Pollution: an Introduction for Students of Engineering and Science. John Wiley and Sons, p. 344.

Hess, S.L., 1959. Introduction to the Theoretical Meteorology. A Holt-Dryden Book. Henry Holt and Company, New York.

Jo, H.-Y., Kim, C.-H., 2013. Identification of long-range transported haze phenomena and their meteorological features over Northeast Asia. J. Appl. Meteorol. Climatol. 52, 1318–1328.

Kim, C.-H., Chang, L.-S., Kim, J.-S., Meng, F., Kajino, M., Ueda, H., Zhang, Y., Son, H.-Y., He, Y., Xu, J., Sato, K., Song, C.-K., Ban, S.-J., Sakurai, T., Han, Z., Duan, L., Lee, S.-J., Shim, S.-G., Sunwoo, Y., Lee, T.-Y., 2011. Long-term simulations of the sulfur concentrations over the China, Japan and Korea: a model comparison study. Asia-Pacific J. Atmos. Sci. 47, 399–411.

Kim, C.-H., Lee, H.-J., Kang, J.-E., Jo, H.-Y., Park, S.-Y., Jo, Y.-J., Lee, J.-J., Yang, G.-H., Park, T., Lee, T., 2018. Meteorological overview and signatures of long-range transport processes during the MAPS-Seoul 2015 campaign. Aerosol Air Qual. Res. 18, 2173–2184.

Kim, C.-H., Meng, F., Kajino, M., Lim, J., Tang, W., Lee, J.-J., Kiriyama, Y., Woo, J.-H., Sato, K., Kitada, T., Minoura, H., Kim, J., Lee, K.-B., Roh, S., Jo, H.-Y., Jo, Y.-J., 2021. Comparative numerical study of $PM_{2.5}$ in exit-and-entrance areas associated with transboundary transport over China, Japan, and Korea. Atmosphere 12 (4), 469.

Kim, C.-H., Park, S.-Y., Kim, Y.-J., Chang, L.-S., Song, S.-K., Moon, Y.-S., Song, C.-K., 2012. A numerical study on indicators of long-range transport potential for anthropogenic particulate matters over northeast Asia. Atmos. Environ. 58, 35–44.

Kim, J., Jeong, U., Ahn, M.-H., Park, R.J., Lee, H., Song, C.H., Choi, Y.-S., Lee, K.-H., Yoo, J.-M., Jeong, M.-J., Park, S.K., Lee, K.-M., Song, C.-K., Kim, S.-W., Kim, Y.J., Kim, S.-W., Kim, M., Go, S., Liu, X., Chance, K., Miller, C.C., Al-Saadi, J., Veihelmann, B., Bhartia, P.K., Torres, O., Abad, G.G., Haffner, D.P., Ko, D.H., Lee, S. H., Woo, J.-H., Chong, H., Park, S.S., Micks, D., Choi, W.J., Moon, K.-J., Veefkind, P., Levelt, P.F., Edwards, D.P., Kang, M., Eo, M., Bak, J., Baek, K., Kwon, H.-A., Yang, J., Park, J., Han, K.M., Kim, B.-R., Shin, H.-W., Choi, H., Lee, E., Chong, J., Cha, Y., Koo, J.-H., Hayashida, S., Kasai, Y., Kanaya, Y., Liu, C., Lin, J., Crawford, J.H., Carmichael, G.R., Newchurch, M.J., Lefer, B.L., Herman, J.R., Swap, R.J., Lau, A.K. H., Kurosu, T.P., Jaross, G., Ahlers, B., Dobber, M., McElroy, T.C., Choi, Y., 2020. New era of air quality monitoring from space: Geostationary Environment Monitoring Spectrometer (GEMS). Bull. Armer. Meteor. Soc. 101, E1–E22.

KMA (Korean Meteorological Administration), 2022. Annual Climatological Report 2021. Korea Meteorological administration (KMA), Seoul. https://data.kma.go.kr/data/publication/publicationAsosList.do?pgmNo=143.

Lee, B., Park, S.U., 1997. Method for forecasting air pollution potential using synoptic meteorological conditions. Asia-Pac. J. Atmos. Sci. 33, 641–656.

Lee, H.-J., Jo, H.-Y., Km, S.-W., Park, M.-S., Kim, C.-H., 2019a. Impacts of atmospheric vertical structures on transboundary aerosol transport from China to South Korea. Sci. Rep. 9, 13040.

Lee, H.-J., Jo, H.-Y., Park, S.-Y., Jo, Y.-J., Jeon, W., Ahn, J.-Y., Kim, C.-H., 2019b. A case study of the transport/transformation of air pollutants over the Yellow Sea during the MAPS 2015 campaign. J. Geophys. Res. Atmos. 124 (12), 6532–6553.

Lee, H.-J., Jo, Y.-J., Kim, S., Kim, D., Kim, J.-M., Choi, D., Jo, H.-Y., Bak, J., Park, S.-Y., Jeon, W., Kim, C.-H., 2022. Transboundary aerosol transport process and its impact on aerosol-radiation-cloud feedbacks in springtime over Northeast Asia. Sci. Rep. 12, 4870.

Lee, H.-J., Kim, S.-W., Brioude, J., Cooper, O.R., Frost, G.J., Kim, C.-H., Park, R.J., Trainer, M., Woo, J.-H., 2014. Transport of NOx in East Asia identified by satellite and in situ measurements and Lagrangian particle dispersion model simulations. J. Geophys. Res. Atmos. 119 (5), 2574–2596.

Levin, Z., Gershon, H., Ganor, E., 2005. Vertical distribution of physical and chemical properties of haze particles in the Dead Sea valley. Atmos. Environ. 39 (27), 4937–4945.

Oh, I.-B., Kim, Y.-K., Hwang, M.-K., Kim, C.-H., Kim, S.-T., Song, S.-K., 2010. Elevated ozone layers over the Seoul metropolitan region in Korea: evidence for long-range ozone transport from Eastern China and its contribution to surface concentrations. J. Appl. Meteorol. Climatol. 49 (2), 203–220.

Park, D.-H., Kim, S.-W., Kim, M.-H., Yeo, H., Park, S.S., Nishizawa, T., Shimizu, A., Kim, C.-H., 2020. Impacts of local versus long-range transported aerosols on PM_{10} concentrations in Seoul, Korea: an estimate based on 11-year PM_{10} and lidar observations. Sci. Total Environ. 750, 141739.

Park, I.-S., Choi, W.-J., Lee, T.-Y., Lee, S.-J., Han, J.-S., Kim, C.-H., 2005. Simulation of long-range transport of air pollutants over Northeast Asia using a comprehensive acid deposition model. Atmos. Environ. 39 (22), 4075–4085.

Peterson, D.A., Hyer, E.J., Han, S.-O., Crawford, J.H., Park, R.J., Holz, R., Kuehn, R.E., Eloranta, E., Knote, C., Jordan, C.E., Lefer, B.L., 2019. Meteorology influencing springtime air quality, pollution transport, and visibility in Korea. Elem. Sci. Anth. 7 (57).

Sanchez, M.L., Pascual, D., Ramos, C., Perez, I., 1990. Forecasting particulate pollutant concentrations in a city from meteorological variables and regional weather patterns. Atmos. Environ. 6, 1509–1519.

Sun, Y., Zhuang, G., Tang, A., Wang, Y., An, Z., 2006. Chemical characteristics of $PM_{2.5}$ and PM_{10} in haze-fog episodes in Beijing. Environ. Sci. Technol. 40 (10), 3148–3155.

Wang, Y., Zhuang, G., Sun, Y., An, Z., 2006. The variation of characteristics and formation mechanisms of aerosols in dust, haze, and clear days in Beijing. Atmos. Environ. 40 (34), 6579–6591.

WMO (World Meteorological Organization), 2022. State of the Global Climate 2021. World Meteorological Organization (WMO), Geneva. https://library.wmo.int/index.php?lvl=notice_display&id=22080#.ZCpyznZByUk.

Zhang, Y., Cooper, O., Gaudel, A., Thompson, A.M., Nédélec, P., Ogino, S.-Y., West, J.J., 2016. Tropospheric ozone change from 1980 to 2010 dominated by equatorward redistribution of emissions. Nat. Geosci. 9, 875–879.

Zhao, C., Tie, X., Wang, G., Qin, Y.U., Yang, P., 2006. Analysis of air quality in eastern China and its interaction with other regions of the world. J. Atmos. Chem. 55 (3), 189–204.